



# NiCoMnO<sub>4</sub> nanoparticles on N-doped graphene: Highly efficient bifunctional electrocatalyst for oxygen reduction/evolution reactions

Afshin Pendashteh <sup>a</sup>, Jesus Palma <sup>a</sup>, Marc Anderson <sup>a,b</sup>, Rebeca Marcilla <sup>a,\*</sup>

<sup>a</sup> Electrochemical Processes Unit, IMDEA Energy Institute, Parque Tecnológico de Móstoles, Avda. Ramón de la Sagra, 3, 28935 Móstoles, Madrid, Spain

<sup>b</sup> Department of Civil and Environmental Engineering, University of Wisconsin, Madison, USA



## ARTICLE INFO

### Article history:

Received 13 June 2016

Received in revised form 11 August 2016

Accepted 16 August 2016

Available online 17 August 2016

### Keywords:

NiCoMnO<sub>4</sub>

Graphene

Electrocatalyst

ORR

OER

## ABSTRACT

Low-cost and highly efficient electrocatalysts for oxygen reactions are of high importance for oxygen-related energy storage/conversion devices (e.g. Metal-O<sub>2</sub> batteries or fuel cells). In the present study, we synthesized NiCoMnO<sub>4</sub> nanoparticles anchored on nitrogen-doped graphene nanosheets as highly efficient bifunctional electrocatalysts for the Oxygen Reduction Reaction (ORR) and for the Oxygen Evolution Reaction (OER). Proper anchoring of NiCoMnO<sub>4</sub> nanoparticles on graphene layers was probed with various characterization techniques including X-ray diffraction, energy dispersive X-ray (EDX), Raman, and Fourier transform infrared (FTIR) spectroscopy as well as transmission electron microscopy (TEM). X-ray photoelectron spectroscopy (XPS) was also employed to shed light on the oxidation states of metallic atoms and types of doped nitrogen on graphene layers. According to the obtained results, the NiCoMnO<sub>4</sub>/N-rGO hybrid showed excellent electrocatalytic activity towards ORR ( $E_{onset} = 0.92$  V vs. RHE and high current density of  $0.84 \text{ mA cm}^{-2}$ ) and OER ( $E_{onset} = 1.5$  V vs. RHE and high current density of  $14 \text{ mA cm}^{-2}$ ), much better than other evaluated catalysts. It has been shown that the NiCoMnO<sub>4</sub>/N-rGO catalyzes ORR mostly through  $4e^-$  process, just as the commercial Pt based catalyst. Moreover, it outperforms the commercial catalyst with very little decay in ORR activity over long continuous operation and shows excellent catalytic selectivity and methanol tolerance.

© 2016 Elsevier B.V. All rights reserved.

## 1. Introduction

The oxygen reduction reaction (ORR) has become one of the most important reactions in energy storage/conversion technologies [1,2]. This reaction is considered as the heart of metal-air batteries since it enables them to achieve large energy densities for a given weight (e.g.  $5200 \text{ Wh kg}^{-1}$  for Li-O<sub>2</sub> or  $1100 \text{ Wh kg}^{-1}$  for Zn-O<sub>2</sub>) [3–5]. While employing atmospheric O<sub>2</sub> makes these devices potentially the most compact and less expensive batteries, sluggish kinetics of oxygen reduction on the cathode necessitates the use of catalysts such as platinum or its alloys to increase the rate of these ORRs. However, the high-cost of Pt and its declining activity for long term performance have triggered plethora of research effort towards developing electrocatalysts based on metal-free or non-precious metals. On the other hand, water oxidation or the companion oxygen evolution reaction (OER) is also critical for rechargeable energy storage applications (e.g. rechargeable aqueous metal-O<sub>2</sub> batteries) [6–9]. However, Pt-based catalysts,

excellent for ORR, show usually poor catalytic activity towards OER which makes using co-catalysts inevitable. Hence, introducing and developing bifunctional catalysts efficient for both ORR and OER is of great demand and is considered as the major challenge towards development and commercialization of metal-air battery and fuel cell technologies. Different types of materials including doped-carbons [10], carbon-transition metal hybrids [11,12], metal-organic-frameworks [13,14], and transition metal oxides [15,16] have been investigated as ORR catalysts in alkaline media, some showing activity towards OER. However, there is still a real need to develop superior, low-cost and bifunctional catalysts. [4,14,17]

Mixed-valence transition metal oxides having a spinel structure are an important category of materials with a broad range of applications as electrode materials in Li-ion batteries, supercapacitors, catalysts, etc [18]. These oxides have a complex composition and the presence of multiple valent states of cations incorporated in these spinel structures empowers them to achieve superior performance in comparison with simple oxides. This multi-valent nature gives them desirable electrocatalytic activity in electrochemical oxygen electrochemistry reactions by providing donor-acceptor chemisorption sites for reversible adsorption

\* Corresponding author.

E-mail address: [Rebeca.marcilla@imdea.org](mailto:Rebeca.marcilla@imdea.org) (R. Marcilla).

of O<sub>2</sub> [18–20]. In particular, spinel cobaltites have attracted great attention as bifunctional oxygen electrodes due to their excellent electrocatalytic activity, ease of preparation, high stability, and low cost [19]. Among all mixed cobalt oxides, NiCoMnO<sub>4</sub> is of interest as electrode material in batteries and supercapacitors due to low Co content, high stability and good electrochemical activity [21–23]. Only recently, Manthiram et al. demonstrated the potential interest of this material as an electrocatalyst by synthesizing NiCoMnO<sub>4</sub>/N-MWCNT nanocomposites and testing their electrocatalytic activity for oxygen reduction and evolution reactions [24]. Their NiCoMnO<sub>4</sub>/N-MWCNT showed good electrocatalytic activity toward ORR with a moderate OER activity in comparison with commercial catalysts. Although these results demonstrate NiCoMnO<sub>4</sub> activity towards oxygen reactions in combination with a carbon support, there is still a large room for improvement and developing catalysts with enhanced catalytic bifunctional activity which can retain this activity over a long time frame. It has been already reported that N-rGO has higher catalytic activity than N-CNTs mainly due to higher surface area and possibility of being heavily doped by nitrogen [25]. Therefore, anchoring NiCoMnO<sub>4</sub> particles on nitrogen-doped graphene as an exceptional active support for oxygen electrochemistry, might be strategically favorable. We believe that this is the first work reporting synthesis of a NiCoMnO<sub>4</sub>/N-rGO hybrid material and its application as a highly efficient bifunctional electrocatalyst for reversible ORR and OER with excellent durability and selectivity.

## 2. Experimental

### 2.1. Synthesis of electrocatalysts

All chemicals were purchased from Sigma-Aldrich and used without any purification. Graphene oxide (GO) was synthesized through a modified Hummers method [26], described elsewhere in detail [21]. For synthesis of NiCoMnO<sub>4</sub>/N-rGO hybrid, 32 mg of GO powder was redispersed in 30 ml of absolute ethanol and subjected to ultrasound irradiation for at least 15 min (Hielscher UP400S ultrasonic processor, Germany) until a stable dispersion was obtained. Next, 1 ml of 0.2 M Ni(CH<sub>3</sub>CO<sub>2</sub>)<sub>2</sub>·4H<sub>2</sub>O, 1 ml of 0.2 M Co(CH<sub>3</sub>CO<sub>2</sub>)<sub>2</sub>·4H<sub>2</sub>O, and 1 ml of Mn(CH<sub>3</sub>CO<sub>2</sub>)<sub>2</sub>·4H<sub>2</sub>O were added to the prepared GO dispersion under vigorous stirring. After 1 h, 2 ml of NH<sub>4</sub>OH solution (28.0–30.0%) was introduced to the mixture of GO and M(CH<sub>3</sub>CO<sub>2</sub>)<sub>2</sub> (M = Ni, Co, or Mn), followed by adding 3 ml of Mili-Q water. The reaction was kept stirring at 80 °C in an oil bath overnight. The mixture then was transferred to a Teflon-lined hydrothermal autoclave reactor (50 ml of total capacity) and the reaction was continued at 150 °C for 3 h. The resulting precipitate was collected by centrifugation at 6000 r.p.m. for 15 min after washing with pure ethanol and Mili-Q water. Finally, the sample was dried at 70 °C overnight. NiCoMnO<sub>4</sub>/rGO nanocomposites were also synthesized via the same route without adding the NH<sub>4</sub>OH solution. Moreover, pure NiCoMnO<sub>4</sub> and N-rGO samples were prepared using a similar approach by excluding GO and M(CH<sub>3</sub>CO<sub>2</sub>)<sub>2</sub> precursors, respectively.

### 2.2. Microstructural characterization of the samples

The prepared samples were structurally characterized using X-ray diffraction (XRD, PANalytical Empyrean diffractometer utilizing Cu K $\alpha$  radiation,  $\lambda = 0.154$  nm) at a generator voltage of 45 kV and an emission current of 40 mA. A Hitachi TM-1000 scanning electron microscope (SEM) and a FEI Tecnai 20 transmission electron microscope (TEM) with a BaF<sub>6</sub> filament at an accelerating voltage of 200 kV were used to investigate morphological properties of the samples. In addition, FEG S/TEM microscope (Talos

F200X, FEI) was used for EDX-STEM mapping experiments. JASCO NRS-5100 Laser Raman and FTIR Nicolet 6700 Thermo Scientific spectrometers were employed to record Raman and FTIR spectra, respectively. Thermal gravimetric analysis (TGA) and differential scanning calorimetry (DSC) of the samples were monitored in air atmosphere between room temperature and 700 °C with a heating rate of 10 °C min<sup>-1</sup> using SDT-Q600 (TA Instruments). X-ray photoelectron spectroscopy (XPS) was conducted to analyze the surface of the NiCoMnO<sub>4</sub>/N-rGO samples by means of a monochromatic Al K $\alpha$  radiation with a voltage of 12 kV, a current of 6 mA, and energy resolution of 0.1 eV for high resolution spectra.

## 2.3. Electrochemical measurements

### 2.3.1. Cyclic voltammetry

4 mg of catalyst and 4 mg of Vulcan carbon were mixed thoroughly and dispersed in 500  $\mu$ l of *N*-Methyl-2-pyrrolidone (NMP) by sonicating the mixture for 30 min in an ultrasonic bath to achieve a homogenous ink. 2  $\mu$ l of the catalyst ink was drop-cast on a glassy carbon electrode (GCE, ALS Co., Japan) yielding a deposit 3 mm in diameter (catalyst mass loading of  $\sim$ 0.225 mg cm<sup>-2</sup>) and subsequently dried at 70 °C for  $\sim$ 30 min. Cyclic voltammetry was conducted in an electrochemical cell vial sealed with Teflon® cap using modified GCE as the working electrode, Pt spring as counter and Saturated Calomel Electrode (SCE, Saturated KCl, ALS, RE-2BP) as reference electrode. All electrochemical measurements were conducted on a *Bio-Logic* (VMP3) multichannel station. Before conducting experiments, the electrolyte (0.1 M KOH) was saturated with pure oxygen or argon (control experiments) by bubbling the gas at into the electrolyte for at least 30 min. In order to ensure gas saturation, purging was continued above the solution during the measurements. Cyclic voltammograms were recorded at a scan rate of 20 mV s<sup>-1</sup> after 5 cycles over a potential range of 0.2 to -0.8 V vs. SCE. Potentials in all electrochemical experiments were transformed into the reversible hydrogen electrode (RHE) scale according to the following equation which stands in 0.1 M KOH:

$$E_{RHE} = E_{SCE} + 0.99 \ln 0.1M KOH \quad (1)$$

*Johnson-Matthey* Pt nominally 20% on carbon black (HiSPEC 3000) was employed as commercial catalyst for comparison [27].

### 2.3.2. Rotating disk electrode (RDE) measurements

The same method described above for CV has been employed for preparing catalysts for RDE measurements. The modified GCE was scanned cathodically at a scan rate of 20 mV s<sup>-1</sup> with various rotating speed from 400 to 2300 r.p.m. using an RRDE-3A (ALS Co., Ltd) apparatus. Koutecky-Levich theory was employed to interpret ORR kinetics and provide a mechanism for this reaction. Accordingly, number of electrons transferred (*n*) was estimated on the basis of following equation [28]:

$$\frac{1}{J} = \frac{1}{J_L} + \frac{1}{J_K} = \frac{1}{B\omega^{1/2}} + \frac{1}{J_K} \quad (2)$$

where *J* is the experimental current density (mA cm<sup>-2</sup>), *J<sub>K</sub>* is kinetic-limiting current density (*J<sub>K</sub> = nFkC<sub>O<sub>2</sub></sub>*), *J<sub>L</sub>* is the diffusion-limiting current density,  $\omega$  is the angular velocity, and *B* can be defined as follows:

$$B = 0.62nFC_{O_2}(D_{O_2})^{2/3}\nu^{-1/6} \quad (3)$$

where *F* is the Faraday constant (96,485 C mol<sup>-1</sup>), *C<sub>O<sub>2</sub></sub>* is the bulk concentration of O<sub>2</sub> ( $1.15 \times 10^{-6}$  mol cm<sup>-3</sup> in 0.1 M KOH), *D<sub>O<sub>2</sub></sub>* is the diffusion coefficient of O<sub>2</sub> ( $1.90 \times 10^{-5}$  cm<sup>2</sup> s<sup>-1</sup>), and *v* is the kinematic viscosity of the electrolyte (0.01 cm<sup>2</sup> s<sup>-1</sup>). For the *Tafel* plot,

the kinetic current has been estimated from the mass-transport correction of RDE using the following equation [1]:

$$J_K = \frac{(J \times J_L)}{(J_L - J)} \quad (4)$$

For stability tests, samples were subjected to chronoamperometric measurements at 0.65 V (ORR) or 1.70 V (OER) vs. RHE at a rotation rate of 1500 r.p.m in O<sub>2</sub> and Ar-saturated 0.1 M KOH solution, respectively. In order to characterize stability of the NiCoMnO<sub>4</sub>/N-rGO sample after electrocatalysis catalyst ink was casted on a graphite sheet, scraped from the substrate after chronoamperometric measurement, and was investigated by XRD and TEM.

### 2.3.3. Rotating ring-disk electrode (RRDE) measurements

The catalyst ink (3 µl), prepared according to the above mentioned recipe, was drop-cast on the surface of a glassy carbon disk (Pt ring/GC disk electrode, ALS Co., Ltd) yielding a deposit of 4 mm in diameter. After drying in an oven at 70 °C for ~30 min, the disk electrode was scanned cathodically at a scan rate of 20 mV s<sup>-1</sup> while a constant potential of 1.49 V vs. RHE was applied to the ring electrode. The number of electrons transferred and percentage of peroxide formation were calculated according to:

$$n = 4 \times \frac{I_D}{I_D + \frac{I_R}{N}} \quad (5)$$

$$\%HO_2^- = 200 \times \frac{\frac{I_R}{N}}{I_D + \frac{I_R}{N}} \quad (6)$$

where I<sub>D</sub> is disk current, I<sub>R</sub> is ring current, and N is the current collection efficiency (N = -I<sub>R</sub>/I<sub>D</sub>) of the Pt ring electrode. N was measured by scanning GC disk electrode from 1.44 to 0.99 V vs. RHE at 20 mV s<sup>-1</sup> and applying a constant potential of 1.44 V to the ring electrode in an aqueous solution of 5 mM K<sub>3</sub>Fe[CN]<sub>6</sub> and 0.1 M KCl [29].

## 3. Results and discussion

### 3.1. Microstructure and composition analysis

During synthesis, an equimolar ratio of metal cations, resulting from hydrolysis of the metal acetates in the ethanol/water solution, were electrostatically attracted to the negatively charged functional groups on the surface of graphene oxide nanosheets. This helps to form a uniform and well distributed nucleation of mixed metal hydroxides which further occurs by aging the solution at 80 °C. By introducing a NH<sub>4</sub>OH solution into the reaction, one not only helps to mediate the nucleation onto the functional groups of GO nanosheets, but also provides a source of nitrogen doping of graphene layers. Subsequently, the hydrothermal process will proceed N-doping, reducing the GO nanosheets and crystallizing the mixed metal oxide spinel onto the N-rGO ([Scheme 1](#)).

XRD was employed to explore crystalline characteristics of the prepared samples. [Fig. 1a](#) shows diffraction patterns of NiCoMnO<sub>4</sub> and NiCoMnO<sub>4</sub>/N-rGO samples. In both specimens, peaks can be well ascribed to the cubic spinel phase of NiCoMnO<sub>4</sub> with Fd3m space group and are in good agreement with previous reports [21–23]. No evidence of any impurities was observed. The NiCoMnO<sub>4</sub>/N-rGO sample exhibited relatively broader peaks, suggesting the formation of smaller crystallites probably due to presence of the graphitic substrate [30]. This was further confirmed by estimating the crystallite size of the particles through Debye-Scherer equation (See Supplementary). Accordingly, an average crystallite size of ~8 nm was obtained for the NiCoMnO<sub>4</sub>/N-rGO hybrid, half the value of the NiCoMnO<sub>4</sub> sample (~16 nm). In addition, a broad, very low-intense peak at around 24° can be

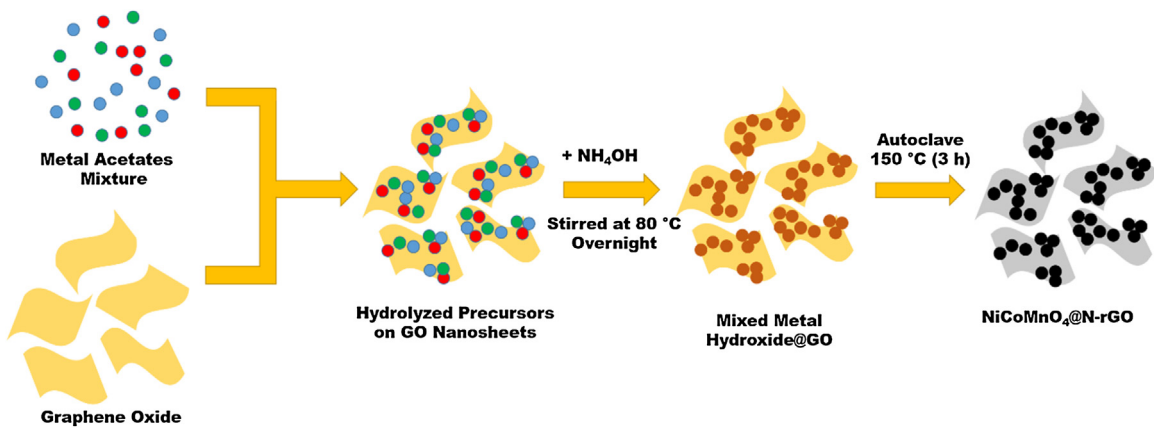
identified in the composite sample, indexed to graphitic plane of (002) of graphene nanosheets. A similar peak could be tracked in the pure N-rGO sample. It has been already observed in previous reports that penetrative growth of metal oxide nanoparticles (NPs) into graphene nanosheets on the basal planes can distort the quasi-periodic restacking of graphene layers, resulting in a lower intensity or diminished (002) peak [31]. Furthermore, no trace of the GO precursor, commonly seen at 2θ = 10°, was detected in NiCoMnO<sub>4</sub>/N-rGO hybrid material, revealing that GO has been heavily reduced while the oxides grew during the hydrothermal reaction. These results clearly demonstrate the successful synthesis of the spinel structure on reduced graphene oxide nanosheets.

To further probe the formation of the hybrid material and its composition, Raman spectroscopy of both pure materials and hybrid sample were performed and shown in [Fig. 1b](#). In the case of N-rGO, the characteristic D and G bands can be clearly seen at 1345 and 1593 cm<sup>-1</sup>, respectively. The G band originates from in-plane vibrations of sp<sup>2</sup> carbons while the D band can be attributed to out of plane vibrations where structural defects exist [32]. As seen in spectrum of pure NiCoMnO<sub>4</sub>, clear peaks appear in the range of 350–1100 cm<sup>-1</sup> which are due to the vibrational modes of M–O bonds [33–35]. Similar peaks with insignificantly changed peak positions can be easily realized in the hybrid material, suggesting that the main components of the hybrid retain similar bulk structures as their individual components. Moreover, a relatively higher I<sub>D</sub>/I<sub>G</sub> ratio was obtained for NiCoMnO<sub>4</sub>/N-rGO hybrid sample (1.28) than for N-rGO (0.98), implying increased structural defects due to inclusion of metal oxide NPs [36].

Fourier-transform infrared (FTIR) spectroscopy was employed to further characterize the samples. As seen in [Fig. 1c](#), carbon characteristic vibrations, including C–N (1198 cm<sup>-1</sup>), C=C (1523 cm<sup>-1</sup>) and C=N (1556 cm<sup>-1</sup>) appear in the range of 4000–800 cm<sup>-1</sup> (mid-infrared) in N-rGO and NiCoMnO<sub>4</sub>/N-rGO samples [37]. Importantly, there is no trace of the strong carboxylic C=O (1720 cm<sup>-1</sup>) peak, seen in the GO sample ([Fig. S1](#)), in N-rGO and NiCoMnO<sub>4</sub>/N-rGO samples, revealing that GO has efficiently reduced during the hydrothermal reaction. For pure NiCoMnO<sub>4</sub> and NiCoMnO<sub>4</sub>/N-rGO samples, two intense absorption bands can be found at 525 and 490 cm<sup>-1</sup> which can be attributed to metal–oxygen vibrations as well as broad peaks of hydroxyl groups at 3410 cm<sup>-1</sup> [38]. The presence of similar peaks in the NiCoMnO<sub>4</sub>/N-rGO composite as in individual components further confirms the coexistence of materials in the hybrid sample.

The mass ratio of components in the hybrid was probed by thermal gravimetric analysis (TGA). [Fig. S2](#) depicts TGA and DSC curves of the NiCoMnO<sub>4</sub>/N-rGO sample up to 700 °C under flowing air. As can be seen in the TGA curve, the sample showed a slight weight loss below 120 °C, ascribed to the evaporation of adsorbed water. After 120 °C, weight loss progressively occurred up to 385 °C. Correspondingly, two clear exothermal peaks were noticed in the DSC results centered at 255 and 350 °C, respectively. The former can be assigned to removal of labile functional groups on surface of the graphene network and the latter can be attributed to the combustion and decomposition of the carbon skeleton. As can be seen, further increase in temperature resulted in no change in sample mass, indicating that around 50 wt.% of nanocomposite corresponds to metal oxide that had been deposited on the graphene network during synthesis.

X-ray photoelectron spectroscopy was utilized to establish elemental composition and chemical oxidation states of metals in the NiCoMnO<sub>4</sub>/N-rGO sample. The overall survey spectrum can be seen in [Fig. 2a](#), indicating the existence of Ni 2p, Co 2p, Mn 2p, O 1s, N 1s, and C 1s in the hybrid material. Accordingly, total content of N in the hybrid sample was estimated to be 2.36 at.%. The high-resolution Ni 2p spectrum ([Fig. 2b](#)) reveals two characteristic peaks centered at 855.8 and 873.8 eV that are attributed to the



**Scheme 1.** Schematic illustration of synthesis of the  $\text{NiCoMnO}_4/\text{N-rGO}$  hybrid material.

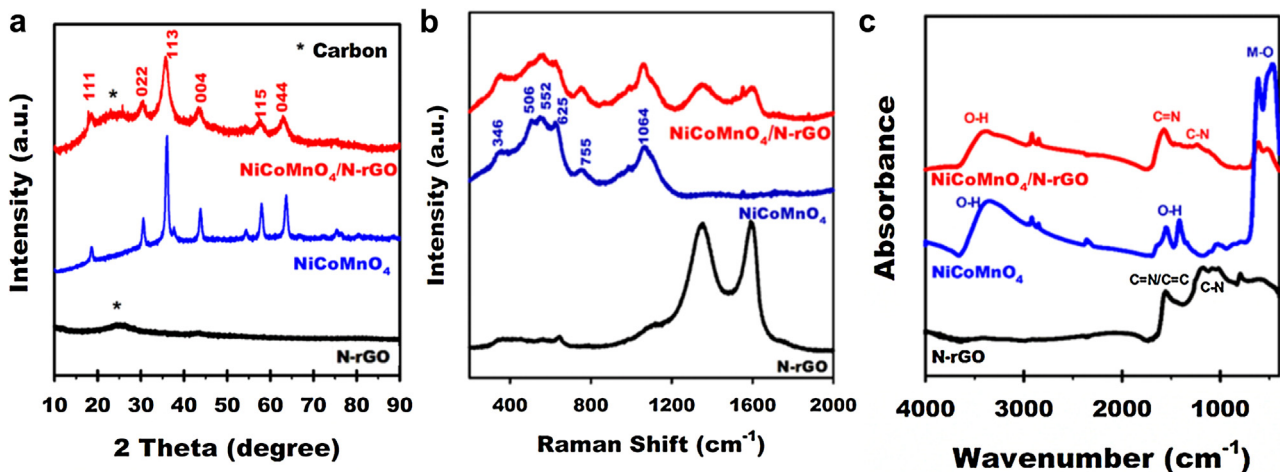


**Fig. 1.** Compositional Characterization of Samples: (a) XRD patterns, (b) Raman and (c) FTIR spectra of N-rGO,  $\text{NiCoMnO}_4$ , and  $\text{NiCoMnO}_4/\text{N-rGO}$  samples.

$\text{Ni}^{2+}$  species [39]. Notable, a satellite has arisen in each case labeled as S1 and S2. Focusing on the high-resolution spectrum of Co 2p core level (Fig. 2c), two clear spin-orbit doublets of Co 2p<sub>3/2</sub> and Co 2p<sub>1/2</sub> can be identified at 780.4 and 795.9 eV, respectively. This is in well agreement with previous reports in the literature, showing a separation of about 15.0 eV [40]. However, the oxidation states of Co cations hardly can be determined only based on the main Co 2p peaks due to similar footmarks in various states. Satellite peaks should also be considered since their energy gap with the main peaks clues in about the oxidation states of the cations. An energy gap of ~6.0 eV stands for  $\text{Co}^{2+}$ , while  $\text{Co}^{3+}$  species result in a gap of 9–10 eV [41,42]. Accordingly, deconvolution of the peaks using Gaussian fitting revealed the presence of  $\text{Co}^{2+}$  and  $\text{Co}^{3+}$  species while  $\text{Co}^{2+}$  is predominant [43]. Fig. 2d depicts high-resolution spectrum of Mn 2p, showing two characteristic spin-orbit doublets with a strong splitting of 11.1 eV which implies the presence of  $\text{Mn}^{3+}$  and  $\text{Mn}^{4+}$  in  $\text{NiCoMnO}_4$  spinel [23]. Deconvolution of N 1s high-resolution peak in Fig. 2e demonstrates the existence of pyridinic (P1), pyrrolic (P2), and graphitic (P3) nitrogen species. As noted, P1-type nitrogens have the greatest contribution in the N 1s peak. This is specially of importance since pyridinic-type nitrogens serve as highly active sites for ORR and have an increasing effect on the activity of catalyst [44]. In Fig. 2f, it can be seen that O 1s spectrum consists of two distinctive peaks emerging at 530.0 eV, corresponding to M–O–M ( $M = \text{Ni}, \text{Co}$ , or  $\text{Mn}$ ) and at 531.7 eV arising from –OH groups [45]. Accordingly, the XPS results are consistent with the expected surface composition, demon-

strating the presence of mixed-valence species in the spinel structure as well as successful hybridization with N-doped reduced graphene oxide.

Growth of  $\text{NiCoMnO}_4$  NPs on N-rGO nanosheets was confirmed through morphological characterization of the hybrid material with transmission electron microscopy (TEM). Fig. 3a and b show TEM images of  $\text{NiCoMnO}_4/\text{N-rGO}$  hybrid, revealing well and uniform distribution of numerous  $\text{NiCoMnO}_4$  NPs supported by graphene layer. It can be seen in Fig. 3b that nanoparticles are homogeneous mostly sphere-shaped with diameter ranging from 5 to 9 nm. This is in agreement with the estimated average particle size from XRD. At a higher-resolution image in Fig. 3c, lattice fringes with an interplanar distance of 0.47 nm can be distinguished, corresponding to (111) crystal plane of  $\text{NiCoMnO}_4$  spinel structure. Elemental composition and purity of the sample was further demonstrated through EDX analysis, shown in the inset of Fig. 3c. A strong Cu signal originates from the polymer-coated copper grid used as the sample holder.

In order to examine how well the elements are distributed in  $\text{NiCoMnO}_4/\text{N-rGO}$  hybrid, STEM elemental mapping was also carried out. Fig. 4 shows TEM image and its corresponding EDX elemental mapping, revealing that the substrate consists of carbon uniformly doped by nitrogen (Fig. 4b, c). It can be clearly seen that metallic elements (Ni, Co, and Mn) are homogeneously distributed in carbon matrix (Fig. 4e–h). In addition, the molar ratio between metals was obtained as nearly 1, further confirming the stoichiometric ratio of  $\text{NiCoMnO}_4$ .

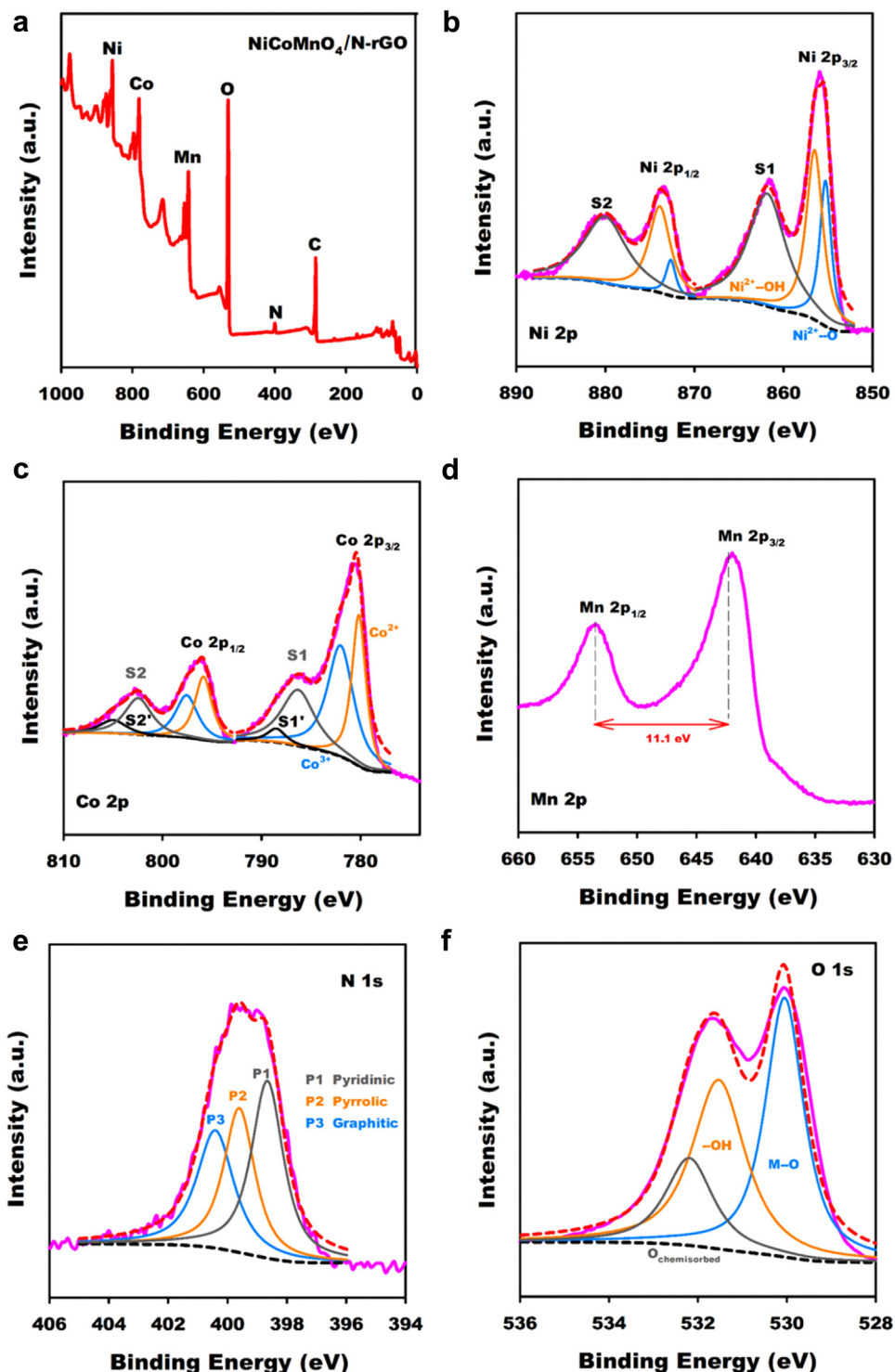


**Fig. 2.** XPS Surface Analysis of  $\text{NiCoMnO}_4/\text{N-rGO}$  Nanocomposite: (a) survey spectrum of  $\text{NiCoMnO}_4/\text{N-rGO}$  nanocomposite, and high-resolution spectra of (b) Ni 2p, (c) Co 2p, (d) Mn 2p, (e) N 1s, and (f) O1s.

### 3.2. Evaluating the electrocatalytic activity of $\text{NiCoMnO}_4/\text{N-rGO}$ hybrid

In order to assess electrocatalytic activity of  $\text{NiCoMnO}_4/\text{N-rGO}$  hybrid material, the catalyst was loaded on GCE (as described in the Experimental section) and subjected to cyclic voltammetry (CV) measurements in  $\text{O}_2$ -saturated 0.1 M KOH solution. For the sake of comparison, similar modified GCE with the same mass loadings were prepared with the pure individual components ( $\text{NiCoMnO}_4$

and N-rGO) and with commercial catalyst (20% Pt/C). Fig. 5a shows CV curves of all samples in a potential range from 1.2 to 0.2 V vs. RHE using a scan rate of  $20 \text{ mV s}^{-1}$ . Control experiments were also conducted in Ar-saturated solutions, shown in dashed lines. It can be seen that in absence of  $\text{O}_2$ , all samples showed almost rectangular CV curves with no clear cathodic redox peak. Conversely, an intense clear redox peak emerged in the cathodic scan for all samples in the presence of  $\text{O}_2$ , revealing catalytic activity of samples toward ORR. Table 1 summarizes oxygen reduction

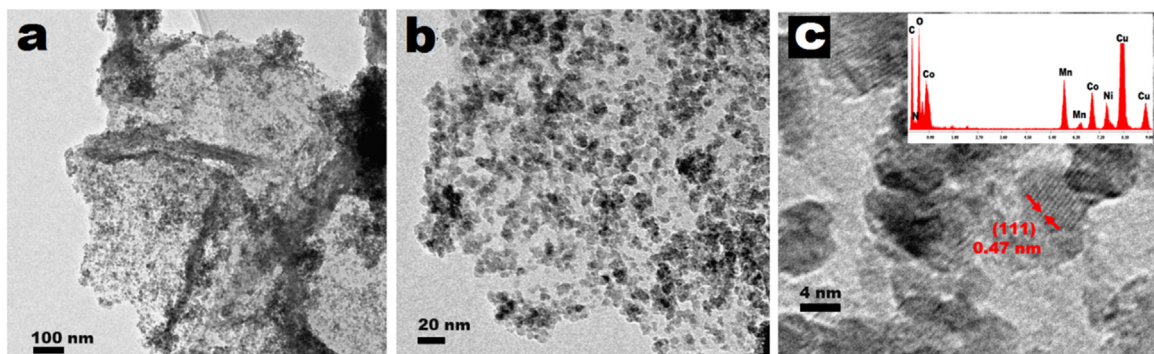


**Fig. 3.** Morphological Characterization of NiCoMnO<sub>4</sub>/N-rGO Hybrid: (a, b) TEM images of NiCoMnO<sub>4</sub>/N-rGO sample at different magnifications. (d) High-resolution TEM image of NiCoMnO<sub>4</sub>/N-rGO hybrid. Inset shows EDX spectrum of the hybrid sample.

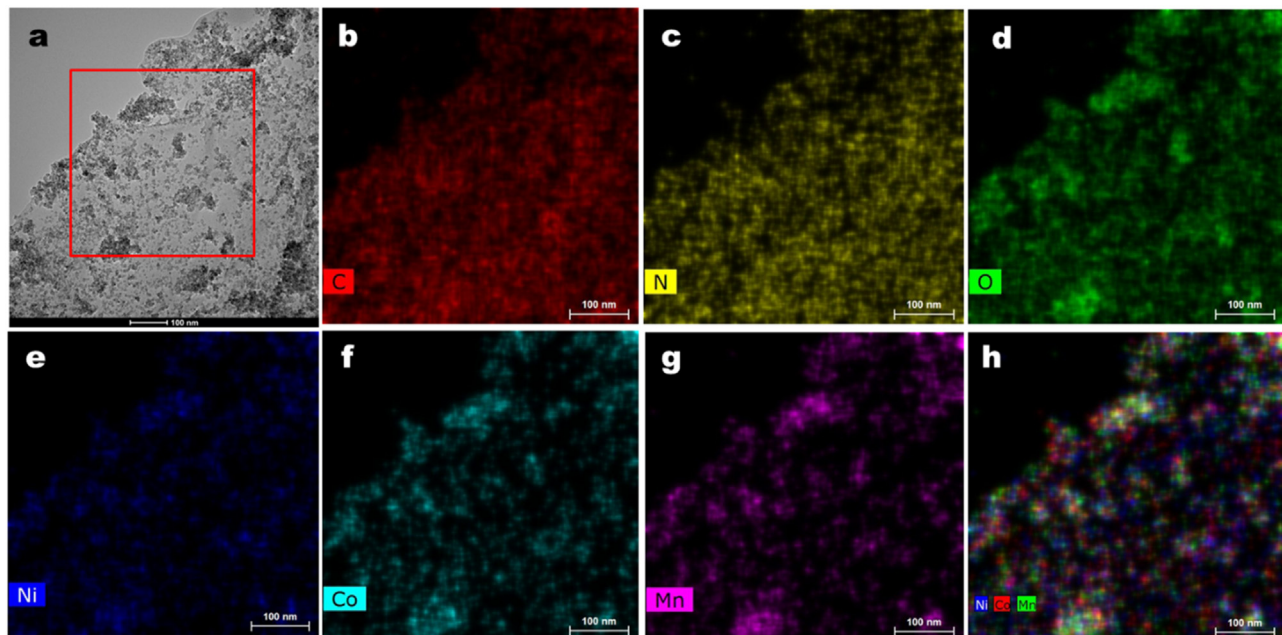


**Fig. 4.** Elemental Mapping of NiCoMnO<sub>4</sub>/N-rGO Hybrid: (a) TEM image and (b-h) corresponding EDX-STEM maps of different elements, showing the distribution of various elements in NiCoMnO<sub>4</sub>/N-rGO Hybrid.

**Table 1**  
Electrochemical parameters extracted from CV curves in Fig. 5a.

Sample	$E_{onset}$ (V vs. RHE)	$E_p$ (V vs. RHE)	$i_p^c$ ( $\text{mA cm}^{-2}$ )
NiCoMnO <sub>4</sub> /N-rGO	0.92	0.75	0.84
NiCoMnO <sub>4</sub>	0.87	0.63	0.54
N-rGO	0.86	0.72	0.56
Pt/C 20%	0.99	0.82	0.52

peak parameters of different samples extracted from Fig. 5a. As can be seen, pure NiCoMnO<sub>4</sub> NPs exhibited a poor ORR catalytic activity with an oxygen reduction peak potential of 0.63 V and a cathodic peak current of  $0.54 \text{ mA cm}^{-2}$ . On the other hand, the N-rGO sample showed certain ORR catalytic activity with a more positive oxygen reduction peak potential (0.72 V) and higher peak current density ( $0.56 \text{ mA cm}^{-2}$ ). Remarkably, NiCoMnO<sub>4</sub>/N-rGO hybrid material showed significantly improved catalytic activity than the individual components, showing an excellent ORR onset potential of 0.92 V (against 0.87 and 0.86 V for NiCoMnO<sub>4</sub> and N-rGO respectively) and much higher peak current density. This can be attributed to the much smaller crystalline particles homogeneously distributed on nitrogen doped graphene layers (confirmed by XRD and TEM) which provides numerous highly active sites for

oxygen reaction as well as arisen synergistic catalytic activity of the components in the hybrid. Moreover, Pt/C 20% as a commercial catalyst was also evaluated. It can be seen that onset peak potential in the NiCoMnO<sub>4</sub>/N-rGO sample (0.92 V) behaves the closest to the commercial catalyst (0.99 V) among all samples. Interestingly, NiCoMnO<sub>4</sub>/N-rGO sample achieved much higher current density ( $0.84 \text{ mA cm}^{-2}$ ) than the Pt/C 20% sample ( $0.52 \text{ mA cm}^{-2}$ ), demonstrating the excellent ORR catalytic activity of the hybrid material. Although the onset potential is comparable with the previous similar reports (e.g.  $E_{onset} = \sim 0.95 \text{ V}$  for NiCoMnO<sub>4</sub>/N-MWCNT), however the NiCoMnO<sub>4</sub>/N-rGO hybrid material provided much superior current densities ( $0.84 \text{ mA cm}^{-2}$  vs.  $\sim 0.55 \text{ mA cm}^{-2}$ ). Furthermore, in order to investigate the role of nitrogen doping in the electrocatalytic activity of the hybrid, similar composite material containing rGO without nitrogen doping (NiCoMnO<sub>4</sub>/rGO) was prepared and their electrocatalytic properties determined and compared with the nitrogen doped sample. As can be seen in Fig. S3a, this sample showed much lower onset potential (0.88 V vs. RHE) and current density ( $0.56 \text{ mA cm}^{-2}$ ) than the NiCoMnO<sub>4</sub>/N-rGO sample, revealing the strong impact of nitrogen doping on the catalytic activity of the composite material. The positive effect of nitrogen doping on catalytic activity has been extensively invest-

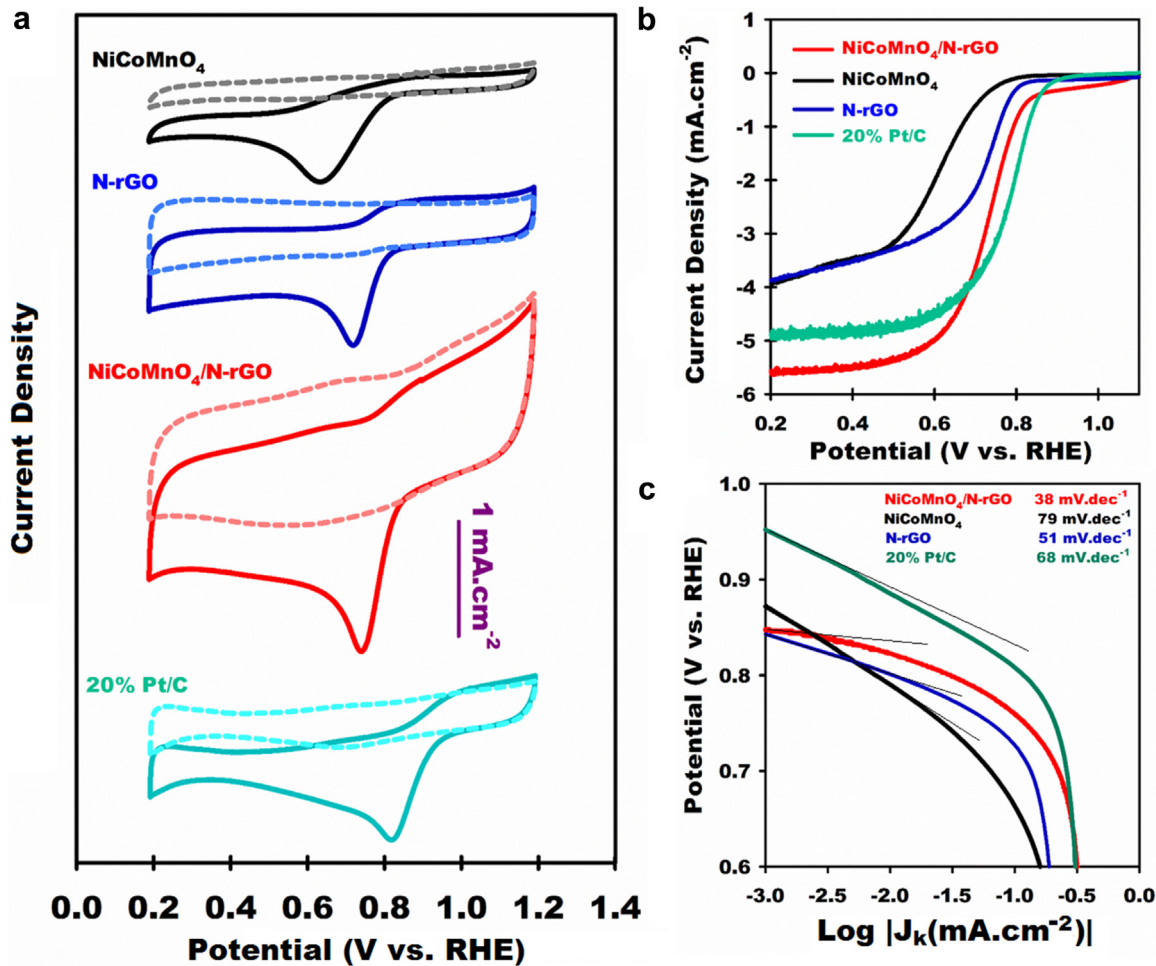


**Fig. 5.** (a) CV curves of NiCoMnO<sub>4</sub>, N-rGO, NiCoMnO<sub>4</sub>/N-rGO, and commercial Pt/C 20% catalysts on glassy carbon electrodes in O<sub>2</sub>-saturated (solid line) or Ar-saturated (dash line) 0.1 M KOH with a scan rate of 20 mV s<sup>-1</sup>. (b) Rotating disk LSV profiles of prepared samples in O<sub>2</sub>-saturated 0.1 M KOH solution at a rotation rate of 1500 r.p.m. with a scan rate of 20 mV s<sup>-1</sup>. (c) Tafel plots of NiCoMnO<sub>4</sub>, N-rGO, NiCoMnO<sub>4</sub>/N-rGO and 20% Pt/C samples derived by the capacitance and mass-transport correction of corresponding RDE data.

tigated and attributed to the increased conductivity and atomic charge density in nitrogen doped materials [46]. Increased charge density in the course of nitrogen doping will result in asymmetry in spin density in the graphene network, facilitating charge transfer from the carbon network to the adsorbing O<sub>2</sub> molecule. This will cause the formation of superoxide ions and weakened O–O bonds which enhance ORR activity by facilitating O–O cleavage [10,47,48].

The improved electrocatalytic activity of NiCoMnO<sub>4</sub>/N-rGO in comparison with the pure components might be due to faster reaction kinetics with a greater number of electrons per O<sub>2</sub> molecule being transferred during ORR. In order to elucidate the ORR mechanism and kinetics in different samples, linear sweep voltammetry (LSV) measurements were performed on rotating-disk electrode (RDE) in O<sub>2</sub>-saturated 0.1 M KOH solutions. Fig. 5b shows LSV curves of various samples recorded at an electrode rotation rate of 1500 r.p.m. with a scan rate of 20 mV s<sup>-1</sup>. The LSV curves of all samples showed an almost single-step plateau at the given r.p.m. However, the plateau in NiCoMnO<sub>4</sub>/N-rGO hybrid is more flat with a small mixed kinetics-diffusion control region, revealing its high catalytic activity. Half-wave potential (E<sub>1/2</sub>) in NiCoMnO<sub>4</sub>/N-rGO shows about 20 and 110 mV shifts in positive potentials as opposed to N-rGO and pure NiCoMnO<sub>4</sub>, respectively. In addition, the half-wave potential (E<sub>1/2</sub>) for the NiCoMnO<sub>4</sub>/N-rGO sample showed approximately a 100 mV positive shift in potential as compared to NiCoMnO<sub>4</sub>-rGO (0.75 against 0.65 V), suggesting that there are

more accessible active sites for ORR in NiCoMnO<sub>4</sub>/N-rGO sample (Fig. S3b). On the other hand, NiCoMnO<sub>4</sub>/N-rGO exhibited extremely higher current density (~1.38 times greater) than the rest of the samples. The greatly improved current density and more positive ORR onset potential in the NiCoMnO<sub>4</sub>/N-rGO sample suggests that the hybridization of NiCoMnO<sub>4</sub> and N-rGO can significantly enhance the electrocatalytic activity in comparison with individual components. Strong electronic coupling of transition metal oxides supported on carbon substrates (e.g. graphene and carbon nanotubes) have already been demonstrated to increase electrocatalytic activity [31,36,49]. In this case, coupling between NiCoMnO<sub>4</sub> and N-rGO might be further enhanced due to strong interaction of the metal sites and doped nitrogen in the graphene substrate which resulted in remarkable improvement in catalytic activity [1,15]. All of these findings are in good agreement with already observed results in CV, illustrating the superior performance of NiCoMnO<sub>4</sub>/N-rGO as an efficient ORR catalyst. This superior performance of this catalyst with respect to ORR electroactivity can be further gleaned from much a smaller Tafel slope of 38 mV dec<sup>-1</sup> at low over-potentials compared to other samples, as shown in Fig. 5c. Smaller Tafel slopes imply that the reaction can attain higher currents at lower over-potentials which further demonstrates the superior catalytic performance of NiCoMnO<sub>4</sub>/N-rGO among various samples.

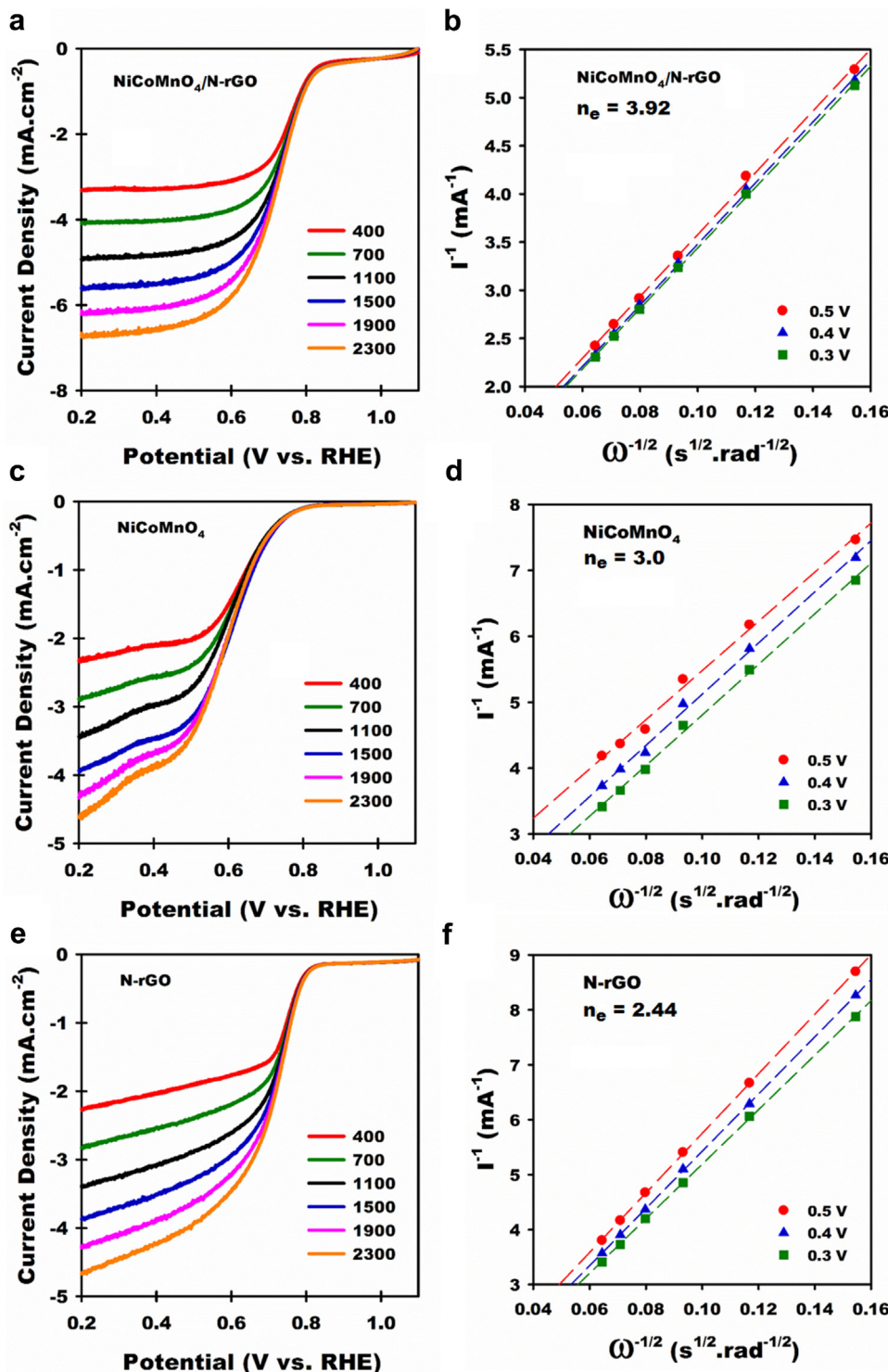
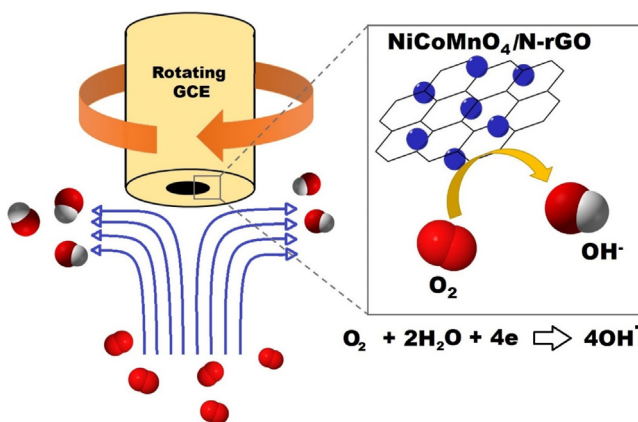


**Fig. 6.** Investigating of ORR Mechanism on Catalysts: (a, c, e) rotating disk LSV profiles of NiCoMnO<sub>4</sub>/N-rGO hybrid, NiCoMnO<sub>4</sub>, and N-rGO samples, respectively in O<sub>2</sub>-saturated 0.1 M KOH solution at various rotation rates ranging from 400 to 2300 r.p.m. with a scan rate of 20 mV s<sup>-1</sup> along with (b, d, f) their corresponding Koutecky-Levich plots at different potentials.

To further unravel the ORR mechanism, *Koutecky-Levich* theory was employed to estimate the number of electrons transferred,  $n$ , during reduction of a single O<sub>2</sub> molecule. To this end, polarization curves of the samples were recorded at various rotation speeds (Fig. 6). As seen in Fig. 6a, the hybrid showed a well-defined increase in cathodic current density in the mixed kinetics-diffusion control region followed by a plateau in the diffusion-limited region. Accordingly, *Koutecky-Levich* curves were plotted at differ-

ent potentials, as shown in Fig. 6b for NiCoMnO<sub>4</sub>/N-rGO. First-order reaction kinetics with respect to the concentration of dissolved oxygen can be understood from linearity of the *Koutecky-Levich* plots. In addition, the parallel behavior of the fitting lines suggest similar electron transfer numbers for ORR at different potentials. From the slope of *Koutecky-Levich* plots, the electron transfer number ( $n$ ) was obtained to be  $\sim 3.92$  at a potential range of 0.50–0.30 V. Similar profiles can be also seen for individual components in Fig. 6c–f.



**Scheme 2.** Schematic illustration of electrocatalytic activity of NiCoMnO<sub>4</sub>/N-rGO hybrid through a 4e pathway.

Calculations for pure NiCoMnO<sub>4</sub> and N-rGO samples resulted in electron transfer number of 3.0 and 2.44, respectively. This clearly indicates that the ORR on NiCoMnO<sub>4</sub>/N-rGO likely follows a 4e mechanistic pathway in a similar fashion as a commercial Pt/C catalyst ( $n \sim 3.99$ , shown in Fig. S4). On the other hand, individual component oxide behave in a mixed mechanistic fashion operating with 2 and 4 electrons.

In order to further probe the exact ORR mechanism taking place with our NiCoMnO<sub>4</sub>/N-rGO hybrid, rotating ring-disk electrode (RRDE) measurements were conducted and peroxide ( $\text{HO}_2^-$ ) formation on the surface of disk was monitored by oxidizing these species on the ring electrode. Fig. 7a shows disk and ring currents for NiCoMnO<sub>4</sub>/N-rGO and commercial Pt/C, recorded at 1500 r.p.m. in 0.1 M KOH at a scan rate of 20 mV s<sup>-1</sup>. As can be seen, NiCoMnO<sub>4</sub>/N-rGO exhibited higher disk currents than the commercial Pt/C catalyst, corresponding to O<sub>2</sub> reduction. However, ring current (peroxide oxidation) in NiCoMnO<sub>4</sub>/N-rGO hybrid is also slightly higher than commercial Pt/C, but still small. This demonstrates that a very small amount of intermediate by-products were produced during ORR on NiCoMnO<sub>4</sub>/N-rGO. Furthermore, the ORR electron transfer numbers and percentage of peroxide species with respect to total ORR products on NiCoMnO<sub>4</sub>/N-rGO were calculated according to equations 5 and 6, respectively. Results obtained are shown in Fig. 7b. As can be seen, the measured HO<sub>2</sub><sup>-</sup> yield is lower than 15% over the potential range of 0.7–0.2 V vs. RHE. Accordingly, an average electron transfer number of 3.79 was achieved which is close to the value obtained from RDE measurements (3.92). It should be mentioned that the value obtained from RRDE experiments are more accurate since the electron transfer number is found by tracking the amount of byproducts in the ORR. These results suggest that the ORR pathway catalyzed by NiCoMnO<sub>4</sub>/N-rGO is mainly through a 4e process by directly forming hydroxyl species as the final products, just as in commercial Pt/C catalysts (Scheme 2).

Stability of NiCoMnO<sub>4</sub>/N-rGO and commercial Pt/C catalysts was tested in a 0.1 M KOH solution using chronoamperometric measurements over a period of 12,500 s (Fig. 8). As seen, NiCoMnO<sub>4</sub>/N-rGO sample exhibits superior durability (~80%) in comparison with the Pt/C catalyst which shows only a 58% current retention. This clearly displays that, while commercial catalyst only provided low long-term ORR currents, our NiCoMnO<sub>4</sub>/N-rGO catalyst could remain stable much longer under the same conditions, demonstrating superior long-term performance of the hybrid catalyst. The excellent catalytic stability of NiCoMnO<sub>4</sub>/N-rGO hybrid is attributed to the sturdy composite structure, as confirmed by XRD (Fig. 8b) and TEM (Fig. 8c, d) after long-term catalysis experiments. As can be seen in Fig. 8b, position, broadness and shape

of the main peaks remained almost unchanged, revealing stable composition, crystallite size and structure of the NiCoMnO<sub>4</sub>/N-rGO sample. Moreover, NiCoMnO<sub>4</sub>/N-rGO hybrid retained its original morphology which further proves stability of the sample during catalytic reaction. As is seen in HRTEM image, crystalline domains and lattice fringes are nearly intact after electrocatalysis which is in excellent agreement with XRD and further supports superb catalytic durability of the hybrid.

Besides catalyst durability, possible fuel crossover effect is also of great importance for an air-cathode catalyst in fuel cell applications. Accordingly, the effect of methanol cross over on catalytic activity of NiCoMnO<sub>4</sub>/N-rGO and commercial Pt/C catalysts was probed by conducting cyclic voltammetry in O<sub>2</sub>-saturated 0.1 M KOH with and without 0.5 M MeOH, as shown in Fig. 9. As can be seen in Fig. 9a, in the case of NiCoMnO<sub>4</sub>/N-rGO hybrid, cyclic voltammogram and current density of ORR peak were remained almost intact, showing an excellent methanol tolerance and catalyst selectivity towards ORR. This is while that the cathodic ORR peak for Pt/C catalyst nearly disappeared and anodic peak related to oxidation of methanol was observed (Fig. 9b). This result further demonstrates promising ORR catalytic properties of NiCoMnO<sub>4</sub>/N-rGO hybrid.

As already mentioned apart from the ORR, the backward reaction, oxygen evolution (OER) is also of great importance for energy storage applications (e.g. metal-air batteries) [50]. To demonstrate the electrocatalytic activity of NiCoMnO<sub>4</sub>/N-rGO towards OER, LSV measurements were conducted by sweeping the potential anodically from 1.1 to 1.8 V (vs. RHE) in 0.1 M KOH solutions with a scan rate of 20 mV s<sup>-1</sup>. Fig. 10a depicts LSV curves for NiCoMnO<sub>4</sub>/N-rGO, and commercial Pt/C catalysts. The NiCoMnO<sub>4</sub>/N-rGO shows an anodic peak at ~1.38 V which can be attributed mainly to the faradaic reaction of Co<sup>3+</sup>/Co<sup>4+</sup> and Mn<sup>3+</sup>/Mn<sup>4+</sup>, located in octahedral sites of the spinel structure. Participation of Co<sup>2+</sup>/Co<sup>3+</sup> and Ni<sup>2+</sup>/Ni<sup>3+</sup> redox couples is also possible but more difficult, as these species sit in tetrahedral sites in the spinel lattice. The quasi-reversible nature of this reaction was demonstrated by CV in Ar (see Fig. S5) where both anodic at 1.38 V and its corresponding cathodic counterpart at 1.26 V are clearly seen. The anodic peak attributed to redox reaction in the catalyst, is followed by the OER onset revealed by a dramatic current increase, showing excellent OER activity of the NiCoMnO<sub>4</sub>/N-rGO hybrid. As can be seen, OER onset potential for NiCoMnO<sub>4</sub>/N-rGO is around 1.5 V, much more negative than the one achieved with commercial Pt/C (~1.63 V) and comparable to previously reported onsets for benchmark IrO<sub>2</sub> (~1.47 V) and RuO<sub>2</sub> catalysts (~1.45 V) [51,52]. This can be due to the fact that NiCoMnO<sub>4</sub> nanoparticles supported on highly conductive nitrogen-doped graphene substrate provide active sites on which charge transfer occurs easily during reaction, lowering the activation energy for O<sub>2</sub> evolution. Additionally, the current density jumped to a maximum value of 14 mA cm<sup>-2</sup>, which is more than 4 times greater than that of commercial Pt/C catalyst. This excellent OER activity of our NiCoMnO<sub>4</sub>/N-rGO hybrid is likely attributed to the high electrical conductivity due to inclusion of nitrogen species in the graphene network and is consistent with improved catalytic activity observed for ORR. Moreover, excellent OER catalytic activity of NiCoMnO<sub>4</sub>/N-rGO was also shown by a much smaller Tafel slope of 128 mV dec<sup>-1</sup>, in comparison with the commercial Pt/C (176 mV dec<sup>-1</sup>) catalyst (Fig. 10b). Electrocatalytic activity stability of the NiCoMnO<sub>4</sub>/N-rGO hybrid towards OER was also examined through chronoamperometric measurements in O<sub>2</sub>-saturated 0.1 M KOH solution at a rotation rate of 1500 r.p.m., over a period of 10,000 s. As seen, NiCoMnO<sub>4</sub>/N-rGO sample could excellently retain around 90% of its initial anodic current after 10,000 s. This is while that Pt/C catalyst shows a current retention of lower 40%.

Table 2 compares the ORR/OER electrocatalytic performance of NiCoMnO<sub>4</sub>/N-rGO hybrid with some recently reported mixed

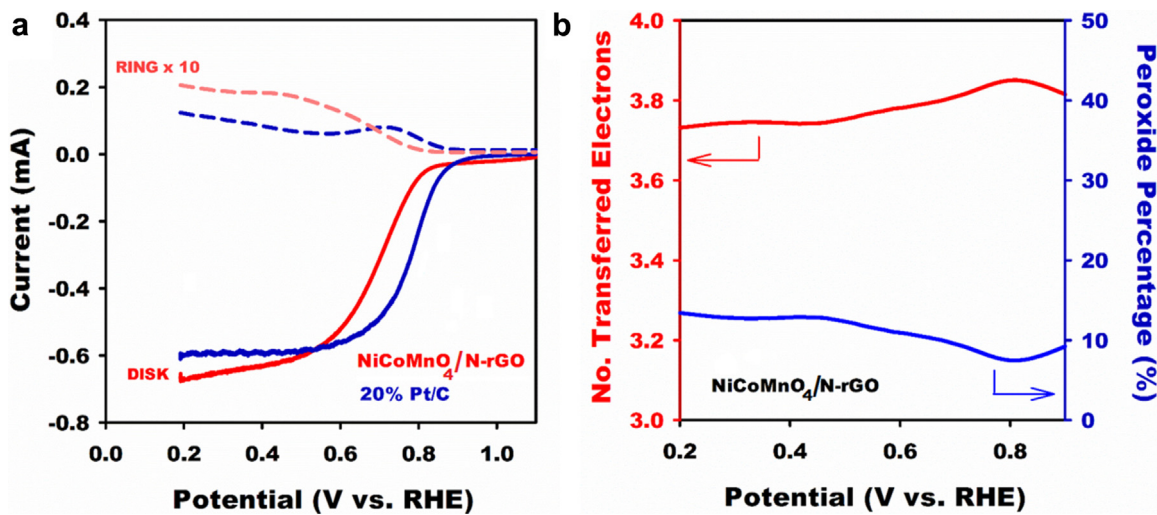


**Fig. 7.** Mechanistic Evaluation of ORR Catalytic Activity NiCoMnO<sub>4</sub>/N-rGO by RRDE: (a) rotating ring-disk electrode (RRDE) LSV profiles of NiCoMnO<sub>4</sub>/N-rGO hybrid and commercial Pt/C 20% in O<sub>2</sub>-saturated 0.1 M KOH solution at a rotation rate of 1500 r.p.m. with a scan rate of 20 mV s<sup>-1</sup>. (b) Percentage of peroxide (blue line) and the electron transfer number (red line) of the NiCoMnO<sub>4</sub>/N-rGO hybrid material at various potentials, based on corresponding RRDE curve. (For interpretation of the references to colour in this figure legend, the reader is referred to the web version of this article.)

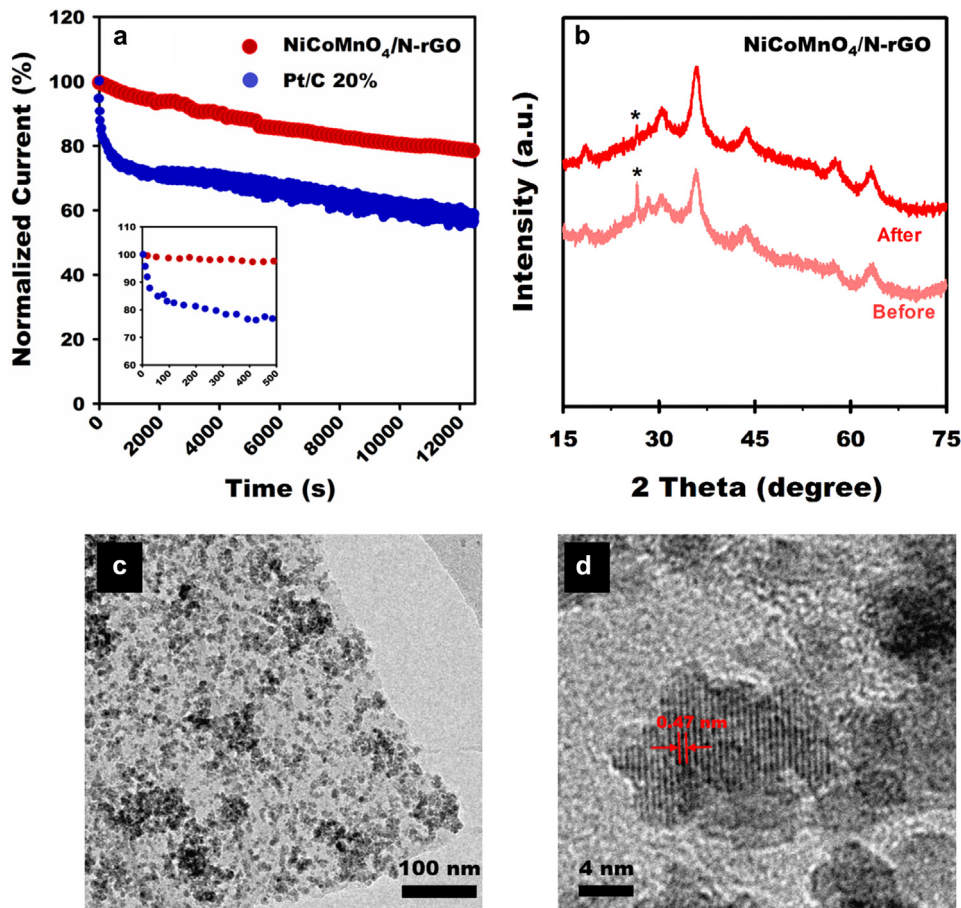


**Fig. 8.** Durability of NiCoMnO<sub>4</sub>/N-rGO Catalyst: (a) Chronoamperometric responses of NiCoMnO<sub>4</sub>/N-rGO hybrid and commercial Pt/C 20% catalysts for 12,500 s at 1500 r.p.m. (b) XRD patterns of NiCoMnO<sub>4</sub>/N-rGO Catalyst before and after long chronoamperometric experiments; sharp peak marked with an asterisk is corresponded to graphite scraped along with the sample. (c, d) TEM images of NiCoMnO<sub>4</sub>/N-rGO sample after electrocatalysis.

spinel oxides and composites. As can be seen, NiCoMnO<sub>4</sub>/N-rGO sample showed superior or comparable catalytic activity, suggesting that NiCoMnO<sub>4</sub>/N-rGO hybrid is an efficient bifunctional ORR/OER electrocatalyst. Specifically, NiCoMnO<sub>4</sub>/N-rGO hybrid outperformed its analogue with MWCNTs in terms of number of

transferred electrons and OER onset potential. This can be due to uniform distribution of mixed transition metal oxide on heavily nitrogen-doped thin layers of graphene which provide a superb active support with high surface area for oxygen electrochemistry. All of the obtained results support the promising catalytic

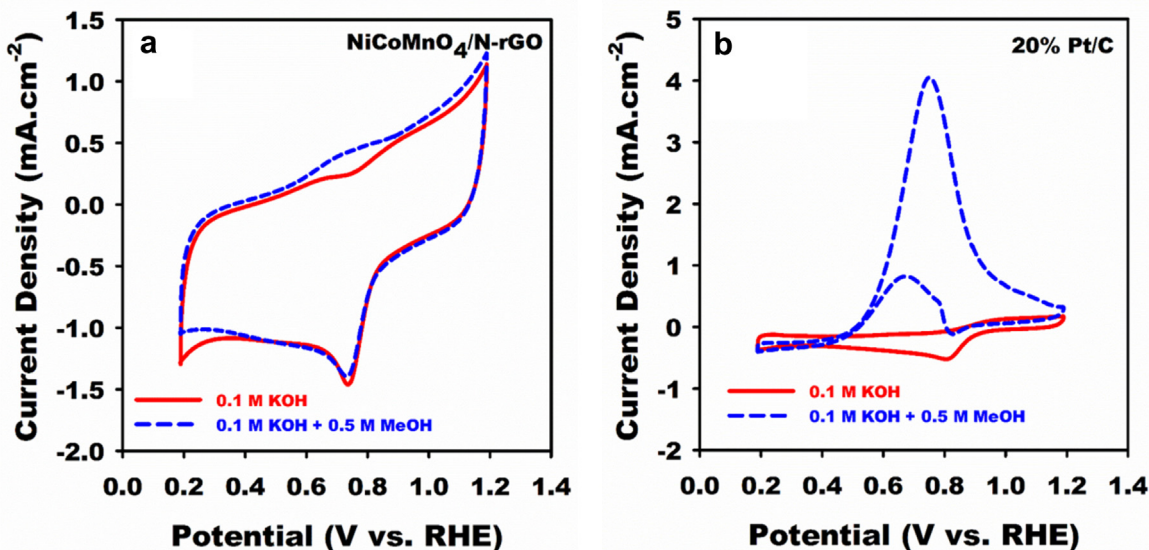


**Fig. 9.** Catalytic Selectivity and Tolerance of Methanol in NiCoMnO<sub>4</sub>/N-rGO Hybrid: (a) CV curves of NiCoMnO<sub>4</sub> and (b) commercial Pt/C 20% catalysts on glassy carbon electrodes in O<sub>2</sub>-saturated 0.1 M KOH (solid line) or 0.1 M KOH + 0.5 M MeOH (dash line) with a scan rate of 20 mV s<sup>-1</sup>.

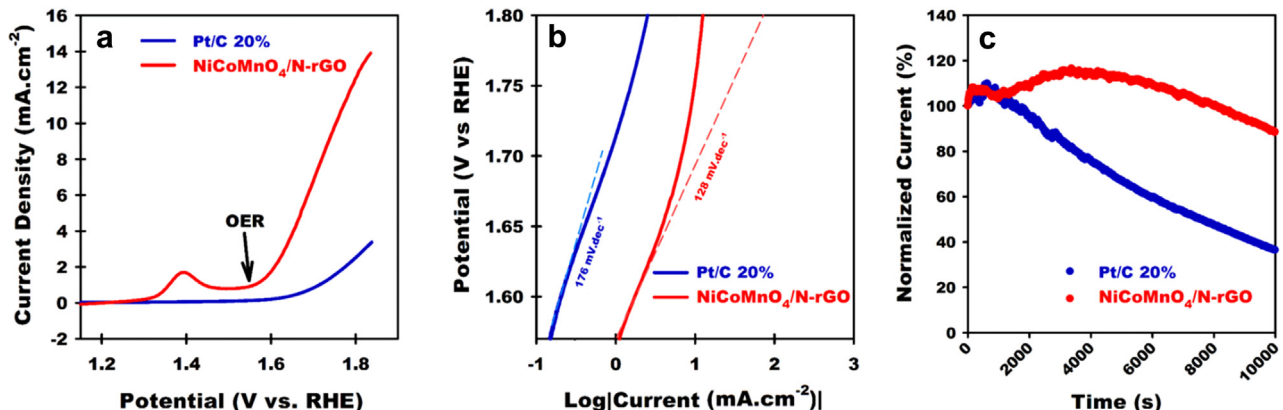


**Fig. 10.** Evaluation of OER Catalytic Activity of Samples: (a) LSV profiles of NiCoMnO<sub>4</sub>/N-rGO and commercial Pt/C 20% catalysts in Ar-saturated 0.1 M KOH with a scan rate of 20 mV s<sup>-1</sup>. (b) Tafel plots of OER for NiCoMnO<sub>4</sub>/N-rGO and commercial catalyst. (c) Chronoamperometric OER catalytic responses of NiCoMnO<sub>4</sub>/N-rGO hybrid and commercial Pt/C 20% for 10,000 s at 1500 r.p.m.

**Table 2**

Comparison of ORR/OER catalytic performance of some recently reported spinel oxides or composites.

Sample	$E_{\text{onset}}^{\text{ORR}}$ (V vs. RHE)	$n_e$	$E_{\text{onset}}^{\text{OER}}$ (V vs. RHE)	Ref.
NiCoMnO <sub>4</sub> /N-rGO	0.92	3.92	1.50	This work
NiCoMnO <sub>4</sub> /N-MWCNT	0.95	3.80	1.55	[24]
CoMn <sub>2</sub> O <sub>4</sub> /N-rGO	0.90	4.00	1.60	[53]
NiCo <sub>2</sub> O <sub>4</sub> /N-rGO	0.87	3.98	—	[15]
MnCo <sub>2</sub> O <sub>4</sub> /N-rGO	0.89	4.00	1.57	[54]
NiCo <sub>2</sub> O <sub>4</sub> /G	0.87	3.90	1.54	[55]
NiCo <sub>2</sub> O <sub>4</sub> Hollow Nanospheres	0.77	3.50	1.45	[56]
NiCo <sub>2</sub> O <sub>4</sub> /CMK-3	0.87	3.85	—	[57]
MnCo <sub>2</sub> O <sub>4</sub> /C Nanosheets	0.94	3.82	—	[58]
CuCo <sub>2</sub> O <sub>4</sub> /N-rGO	0.85	3.80	—	[59]
FeCo <sub>2</sub> O <sub>4</sub> /Hollow Graphene Spheres	0.89	3.92	1.66	[60]
Porous ZnCo <sub>2</sub> O <sub>4</sub> Microspheres	0.86	3.83	—	[61]

characteristics of NiCoMnO<sub>4</sub>/N-rGO as an efficient non-precious bifunctional electrocatalyst for reversible oxygen reduction or evolution reactions with excellent durability and selectivity.

#### 4. Conclusion

In summary, we have synthesized well distributed NiCoMnO<sub>4</sub> spinel nanoparticles on N-doped reduced graphene oxide via a

facile hydrothermal route and investigated their electrocatalytic activity for oxygen reduction (ORR) and evolution (OER) reactions. According to the obtained results, this NiCoMnO<sub>4</sub>/N-rGO hybrid outperformed pure NiCoMnO<sub>4</sub> and N-rGO, in terms of much more positive onset potentials and cathodic current densities for ORR. Rotating disk (RDE) and ring-disk electrode (RRDE) measurements verified that NiCoMnO<sub>4</sub>/N-rGO catalyzes ORR mainly from a 4e process, the same mechanism as has been found in

commercial Pt/C catalysts. Moreover, the NiCoMnO<sub>4</sub>/N-rGO hybrid catalyst showed superior durability (~80%) against a commercial catalyst which decayed very fast (59% retention). Furthermore, we evaluated electrocatalytic activity of NiCoMnO<sub>4</sub>/N-rGO for oxygen evolution reaction (OER), demonstrating excellent behavior and durability. These results suggest NiCoMnO<sub>4</sub>/N-rGO as an efficient non-precious metal-based bifunctional catalyst for oxygen-based energy storage applications.

## Acknowledgements

Authors gratefully acknowledge financial support from the European Commission through *Marie-Curie AMAROUT II* Fellowship program (A.P.), MINECO (former MICINN) through the *Ramon y Cajal* Program (RYC-2011-08093), ENE2012-31516, MAT2015-64167-C2-1-R, European Union structural funds and the Comunidad de Madrid MAD2D-CM Program (S2013/MIT-3007). Authors are also thankful to Dr Fernando Picó for helping through the structural and morphological characterization of the samples.

## Appendix A. Supplementary data

Supplementary data associated with this article can be found, in the online version, at <http://dx.doi.org/10.1016/j.apcatb.2016.08.044>.

## References

- [1] Y. Liang, Y. Li, H. Wang, J. Zhou, J. Wang, T. Regier, H. Dai, *Nat. Mater.* 10 (2011) 780–786.
- [2] X. Ge, A. Sumboja, D. Wuu, T. An, B. Li, F.W.T. Goh, T.S.A. Hor, Y. Zong, Z. Liu, *ACS Catal.* 5 (2015) 4643–4667.
- [3] M.A. Rahman, X. Wang, C. Wen, *J. Electrochem. Soc.* 160 (2013) A1759–A1771.
- [4] Y. Liang, H. Wang, J. Zhou, Y. Li, J. Wang, T. Regier, H. Dai, *J. Am. Chem. Soc.* 134 (2012) 3517–3523.
- [5] R. Cao, J.-S. Lee, M. Liu, J. Cho, *Adv. Energy Mater.* 2 (2012) 816–829.
- [6] M. Xu, D.G. Ivey, Z. Xie, W. Qu, *J. Power Sources* 283 (2015) 358–371.
- [7] Y. Li, M. Gong, Y. Liang, J. Feng, J.-E. Kim, H. Wang, G. Hong, B. Zhang, H. Dai, *Nat. Commun.* 4 (2013) 1805.
- [8] S. Narayan, A. Manohar, S. Mukerjee, *Electrochem. Soc. Interface* 24 (2015) 65–69.
- [9] L. Han, X.-Y. Yu, X.W. Lou, *Adv. Mater.* 28 (2016) 4601–4605.
- [10] Z. Chen, D. Higgins, H. Tao, R.S. Hsu, Z. Chen, *J. Phys. Chem. C* 113 (2009) 21008–21013.
- [11] Y. Liu, H. Jiang, Y. Zhu, X. Yang, C. Li, *J. Mater. Chem. A* 4 (2016) 1694–1701.
- [12] T. Sun, L. Xu, S. Li, W. Chai, Y. Huang, Y. Yan, J. Chen, *Appl. Catal. B* 193 (2016) 1–8.
- [13] H. Hu, L. Han, M. Yu, Z. Wang, X.W. Lou, *Energy Environ. Sci.* 9 (2016) 107–111.
- [14] B.Y. Xia, Y. Yan, N. Li, H.B. Wu, X.W. Lou, X. Wang, *Nat. Energy* 1 (2016) 15006.
- [15] H. Zhang, H. Li, H. Wang, K. He, S. Wang, Y. Tang, J. Chen, *J. Power Sources* 280 (2015) 640–648.
- [16] G. Zhang, B.Y. Xia, X. Wang, X.W. Lou, *Adv. Mater.* 26 (2014) 2408–2412.
- [17] K.A. Stoerzinger, M. Risch, B. Han, Y. Shao-Horn, *ACS Catal.* 5 (2015) 6021–6031.
- [18] C. Yuan, H.B. Wu, Y. Xie, X.W. Lou, *Angew. Chem. Int. Ed.* 53 (2014) 1488–1504.
- [19] M. Hamdani, R. Singh, P. Chartier, *Int. J. Electrochem. Sci.* 5 (2010) 556.
- [20] F. Cheng, J. Shen, B. Peng, Y. Pan, Z. Tao, J. Chen, *Nat. Chem.* 3 (2011) 79–84.
- [21] A. Pendashteh, J. Palma, M. Anderson, R. Marcilla, *RSC Adv.* 6 (2016) 28970–28980.
- [22] Y. Ren, Z. Ma, P.G. Bruce, *J. Mater. Chem.* 22 (2012) 15121–15127.
- [23] K. Li, X. Luo, X. Lin, F. Qi, P. Wu, *J. Mol. Catal. A: Chem.* 383–384 (2014) 1–9.
- [24] X. Yu, A. Manthiram, *Catal. Sci. Technol.* 5 (2015) 2072–2075.
- [25] Y. Zhang, W.-J. Jiang, X. Zhang, L. Guo, J.-S. Hu, Z. Wei, L.-J. Wan, *PCCP* 16 (2014) 13605–13609.
- [26] W.S. Hummers, R.E. Offeman, *J. Am. Chem. Soc.* 80 (1958) 1339.
- [27] E.E. Said-Galiyev, A.Y. Nikolaev, E.E. Levin, E.K. Lavrentyeva, M.O. Gallyamov, S.N. Polyakov, G.A. Tsirlina, O.A. Petrii, A.R. Khokhlov, *J. Solid State Electrochem.* 15 (2011) 623–633.
- [28] M. Sun, Y. Dong, G. Zhang, J. Qu, J. Li, *J. Mater. Chem. A* 2 (2014) 13635–13640.
- [29] C. Pozo-Gonzalo, O. Kartachova, A.J. Torriero, P.C. Howlett, A.M. Glushenkov, D.M. Fabijanic, Y. Chen, S. Poissonnet, M. Forsyth, *Electrochim. Acta* 103 (2013) 151–160.
- [30] T.S. Sahu, S. Mitra, *Sci. Rep.* 5 (2015) 12571.
- [31] K.-H. Wu, Q. Zeng, B. Zhang, X. Leng, D.-S. Su, I.R. Gentle, D.-W. Wang, *ChemSusChem* 8 (2015) 3331–3339.
- [32] F. Banhart, J. Kotakoski, A.V. Krasheninnikov, *ACS Nano* 5 (2011) 26–41.
- [33] C. Luo, D. Li, W. Wu, Y. Zhang, C. Pan, *RSC Adv.* 4 (2014) 3090–3095.
- [34] Z.-Q. Liu, K. Xiao, Q.-Z. Xu, N. Li, Y.-Z. Su, H.-J. Wang, S. Chen, *RSC Adv.* 3 (2013) 4372–4380.
- [35] D. Li, Y. Gong, Y. Zhang, C. Luo, W. Li, Q. Fu, C. Pan, *Sci. Rep.* 5 (2015) 12903.
- [36] M. Sun, H. Liu, Y. Liu, J. Qu, J. Li, *Nanoscale* 7 (2015) 1250–1269.
- [37] S. Deng, C. Thomas Cherian, X.I. Liu, H.R. Tan, L.H. Yeo, X. Yu, A. Rusydi, B.V.R. Chowdari, H.M. Fan, C.H. Sow, *Chem.—Eur. J.* 20 (2014) 12444–12452.
- [38] M. Srivastava, M. Elias Uddin, J. Singh, N.H. Kim, J.H. Lee, *J. Alloys Compd.* 590 (2014) 266–276.
- [39] J. Ji, L.L. Zhang, H. Ji, Y. Li, X. Zhao, X. Bai, X. Fan, F. Zhang, R.S. Ruoff, *ACS Nano* 7 (2013) 6237–6243.
- [40] D. Barreca, C. Massignan, S. Daolio, M. Fabrizio, C. Piccirillo, L. Armelao, E. Tonello, *Chem. Mater.* 13 (2001) 588–593.
- [41] W. Wei, W. Chen, D.G. Ivey, *Chem. Mater.* 20 (2008) 1941–1947.
- [42] S. Wang, Y. Hou, X. Wang, *ACS Appl. Mater. Interfaces* 7 (2015) 4327–4335.
- [43] A. Pendashteh, J. Palma, M. Anderson, R. Marcilla, *J. Mater. Chem. A* 3 (2015) 16849–16859.
- [44] C.V. Rao, C.R. Cabrera, Y. Ishikawa, *J. Phys. Chem. Lett.* 1 (2010) 2622–2627.
- [45] L. An, L. Huang, P. Zhou, J. Yin, H. Liu, P. Xi, *Adv. Funct. Mater.* 25 (2015) 6814–6822.
- [46] E. Bayram, G. Yilmaz, S. Mukerjee, *Appl. Catal. B* 192 (2016) 26–34.
- [47] Z.-S. Wu, S. Yang, Y. Sun, K. Parvez, X. Feng, K. Müllen, *J. Am. Chem. Soc.* 134 (2012) 9082–9085.
- [48] D. Guo, R. Shibuya, C. Akiba, S. Saji, T. Kondo, J. Nakamura, *Science* 351 (2016) 361–365.
- [49] Y. Ma, H. Wang, J. Key, V. Linkov, S. Ji, X. Mao, Q. Wang, R. Wang, *Int. J. Hydrogen Energy* 39 (2014) 14777–14782.
- [50] M.Y. Song, D.-S. Yang, K.P. Singh, J. Yuan, J.-S. Yu, *Appl. Catal. B* 191 (2016) 202–208.
- [51] Y. Zhu, W. Zhou, Y. Chen, J. Yu, M. Liu, Z. Shao, *Adv. Mater.* 27 (2015) 7150–7155.
- [52] X. Liu, J. Jiang, L. Ai, *J. Mater. Chem. A* 3 (2015) 9707–9713.
- [53] M. Prabu, P. Ramakrishnan, S. Shanmugam, *Electrochim. Commun.* 41 (2014) 59–63.
- [54] X. Ge, Y. Liu, F.W.T. Goh, T.S.A. Hor, Y. Zong, P. Xiao, Z. Zhang, S.H. Lim, B. Li, X. Wang, Z. Liu, *ACS Appl. Mater. Interfaces* 6 (2014) 12684–12691.
- [55] D.U. Lee, B.J. Kim, Z. Chen, *J. Mater. Chem. A* 1 (2013) 4754–4762.
- [56] J. Wang, Y. Fu, Y. Xu, J. Wu, J.-H. Tian, R. Yang, *Int. J. Hydrogen Energy* 41 (2016) 8847–8854.
- [57] X. Bo, Y. Zhang, M. Li, A. Nsabimana, L. Guo, *J. Power Sources* 288 (2015) 1–8.
- [58] G. Fu, Z. Liu, J. Zhang, J. Wu, L. Xu, D. Sun, J. Zhang, Y. Tang, P. Chen, *Nano Res.* 9 (2016) 2110–2122.
- [59] R. Ning, J. Tian, A.M. Asiri, A.H. Qusti, A.O. Al-Youbi, X. Sun, *Langmuir* 29 (2013) 13146–13151.
- [60] W. Yan, Z. Yang, W. Bian, R. Yang, *Carbon* 92 (2015) 74–83.
- [61] H. Wang, X. Song, H. Wang, K. Bi, C. Liang, S. Lin, R. Zhang, Y. Du, J. Liu, D. Fan, Y. Wang, M. Lei, *Int. J. Hydrogen Energy* 41 (2016) 13024–13031.